HHS Public Access

Author manuscript

Mol Cancer Res. Author manuscript; available in PMC 2022 April 01.

Published in final edited form as:

Mol Cancer Res. 2021 October ; 19(10): 1739–1750. doi:10.1158/1541-7786.MCR-21-0005.

Radium-223-induced bystander effects cause DNA damage and apoptosis in disseminated tumor cells in bone marrow

Brian S. Canter[1], **Calvin N. Leung**[1], **J. Christopher Fritton**[2], **Tom Bäck**[3], **Didier Rajon**[4], **Edouard I. Azzam**[1,5], **Roger W. Howell**[1]

[1]Department of Radiology, New Jersey Medical School, Rutgers University, Newark, NJ USA;

[2]Departments of Mechanical and Biomedical Engineering, City College of New York, New York, NY USA;

[3]Department of Radiation Physics, The Sahlgrenska Academy, University of Gothenburg, Gothenburg, Sweden;

[4]Department of Neurosurgery, University of Florida, Gainesville, FL USA;

[5]Radiobiology and Health Branch, Canadian Nuclear Laboratories, Chalk River, ON, Canada.

Abstract

Radiation-induced bystander effects have been implicated in contributing to the growth delay of disseminated tumor cells (DTC) caused by $^{223}RaCl_2$, an alpha particle emitting radiopharmaceutical. To understand how $^{223}RaCl_2$ affects the growth, we have quantified biological changes caused by direct effects of radiation and bystander effects caused by the emitted radiations on DTC and osteocytes. Characterizing these effects contribute to understanding the efficacy of alpha particle emitting radiopharmaceuticals and guide expansion of their use clinically. MDA-MB-231 or MCF-7 human breast cancer cells were inoculated intratibially into nude mice that were previously injected intravenously with 50 or 600 kBq/kg $^{223}RaCl_2$. At 1- and 3-days postinoculation, tibiae were harvested and examined for DNA damage (γ-H2AX foci) and apoptosis in osteocytes and cancer cells located within and beyond the range (70 μm) of alpha particles emitted from the bone surface. Irradiated and bystander MDA-MB-231 and MCF-7 cells harbored DNA damage. Bystander MDA-MB-231 cells expressed DNA damage at both treatment levels while bystander MCF-7 cells required the higher administered activity. Osteocytes also had DNA damage regardless of inoculated cancer cell line. The extent of DNA damage was quantified by increases in low (1–2 foci), medium (3–5 foci), and high (5+ foci) damage. MDA-MB-231 but not MCF-7 bystander cells showed increases in apoptosis in $^{223}RaCl_2$ treated animals, as did irradiated osteocytes. Radiation-induced bystander effects contribute to DTC-cytotoxicity caused

Corresponding Author: Roger W. Howell, Professor, Division of Radiation Research, Department of Radiology and Center for Cell Signaling, New Jersey Medical School, Rutgers University, 205 S. Orange Avenue, Newark, NJ 07103, USA, Tel: 973-972-5067, rhowell@rutgers.edu.

Authorship

Contribution: CNL handled and treated mice. BSC assisted with tissue harvest. BSC processed and sectioned tissue, stained sections, and imaged. BSC quantified tissue sections with guidance from RWH, EIA and JCF who also assisted in the design of experiments. BSC and RWH analyzed data. BSC prepared figures and drafted the paper. DR and TB along with all authors helped edit manuscript.

Conflict of Interest Disclosure: The authors declare no potential conflicts of interest.

by $^{223}RaCl_2$. Implications: This observation supports clinical investigation of the efficacy of $^{223}RaCl_2$ to prevent breast cancer DTC from progressing to oligometastases.

Keywords

radiation; alpha particle; bystander effect; breast cancer; bone

Introduction:

Metastatic breast cancer severely compromises the life expectancy of patients. Breast cancer cells detach from the primary tumor and become circulating tumor cells (CTC), and then disseminate to various tissues in the body. These disseminated tumor cells (DTC) (1) often reside in the bone marrow, lie dormant, and eventually form skeletal metastases. An emerging candidate for treating DTC is radium-223 dichloride ($^{223}RaCl_2$), an alpha particle emitting radiopharmaceutical that localizes preferentially to bone. $^{223}RaCl_2$ is USFDA-approved for treatment of castrate resistant prostate cancer that has metastasized to bone (2). It is the only bone seeking treatment that has increased overall survival of advanced stage prostate cancer patients (3). Due to their short range (<100 μm), alpha particles are ideal for sparing bone marrow cells (4,5). Alpha particles are high linear energy transfer (LET) radiation with densely ionizing tracks that create complex DNA damage and increase the frequency of non-rejoining DNA double strand breaks in DTC (6).

The uptake of $^{223}RaCl_2$ by bone is fast and unbound material is cleared rapidly. This is followed by very slow biological clearance from bone, and progeny radionuclides remain largely in equilibrium with the parent ^{223}Ra (4,7). Because of this long retention, and its resulting chronic irradiation, bone can accumulate mean absorbed doses in the range of tens of Gy, which is typical for therapeutic administered activities (4). Past studies that examined the effect of $^{223}RaCl_2$ on bone cells have focused on bone forming osteoblasts and bone resorbing osteoclasts with both suffering DNA damage and population-decrease in the femurs of mice treated with $^{223}RaCl_2$ (8,9). However, the effect of $^{223}RaCl_2$, and more generally alpha particles, on osteocytes in bone is not well known (5,10).

Osteocytes are the master regulators of bone homeostasis (11). Osteocytes originate from osteoblasts embedded in bone matrix. Their dendritic processes interconnect osteocytes with one another and with osteoblasts on the bone surface (12). They also interconnect osteocytes with marrow space and blood vessels (13,14). Osteocytes have an emerging role in bone and non-bone diseases, including cancer, leading to greater interest in therapeutics that specifically target them (15,16). The impact of osteocytes on DTC, and *vice versa*, is poorly defined. Recent investigations uncovered that osteocytes can both provide a hospitable environment for DTC and influence their proliferation (16,17). Much of the work examining biological changes in osteocytes in the presence of breast cancer cells has been performed in a variety of *in vitro* models (18). The dynamic nature of osteocytes, their potential influence on the tumor microenvironment, and their location in irradiated bone tissue all point to the need to investigate their response to $^{223}RaCl_2$ *in vivo*.

Beyond inducing changes through direct irradiation, alpha particles also induce cytotoxicity in unirradiated neighboring cells via radiation-induced bystander effects (19). Similar to the investigation of dynamics between osteocytes and DTC, the bystander effect has been investigated extensively *in vitro* (20–24), however, there are limited *in vivo* studies utilizing alpha-particle emitters (25–29). We recently created an *in vivo* bystander DTC-model by first injecting mice intravenously with $^{223}RaCl_2$, followed by intratibial inoculation of MCF-7 or MDA-MB-231 human breast cancer cells (30). Both cell lines experienced growth delay, however MCF-7 was affected more robustly. Histological analysis of the tibial marrow, dosimetry using Monte Carlo radiation transport modeling, and alpha camera imaging together revealed that many DTC were outside the range of the alpha particles emitted by $^{223}RaCl_2$. The disparate responses of the two cell lines, despite similar radiosensitivity and location in the marrow compartment, suggested that direct radiation effects alone could not explain the differences; therefore, radiation-induced bystander effects are likely to have played a role in the growth delay (30). The present study was undertaken to quantify induced bystander effects using direct measurements of responses in irradiated and bystander DTC. Specifically, we used *in situ* histological methods to assess DNA damage and apoptosis of tibial DTC and osteocytes caused by $^{223}RaCl_2$. The measurements in DTC were made in two distinct populations of cells in the tibia, namely those beyond the range of alpha particles (*i.e.*, bystander cells) and those directly irradiated by alpha particles.

Materials and Methods:

Cell culture and animals

MCF-7-*luc*-F5 estrogen receptor positive (ER+) and MDA-MB-231-*luc*-D3H1 triple negative (ER-, PR-, Her2/neu-) human breast cancer cells were acquired from Caliper Life Sciences. Both cell lines were cultured in Leibovitz L-15 medium (Sigma Aldrich) with 10% fetal bovine serum (Gibco #10437, lot #539574), 2 mM L-glutamine (Gibco #25-030-081) and 100 IU/mL penicillin and 100 μg/mL streptomycin (Corning #MT30002CL). Cells were passaged weekly upon reaching 80–90% confluency in T-175 flasks (Corning) for no more than 1.5 months. Cells were not tested for mycoplasma. Both cell lines were authenticated using Short Tandem Repeat analysis by ATCC on 8/20/2015 and aliquots frozen in liquid nitrogen for subsequent use (30).

Female Fox1^{nu} athymic nude mice (4–6 weeks old, 18–23 g, Envigo) were housed in rectangular opaque M.I.C.E. cages in groups of 4–5 on wooden shavings. Mice were provided with food (PicoLab Rodent Diet 20 (LabDiet)) and water *ad libitum* and acclimated for 1 wk. They were subjected to a 12-h light dark/cycle. All procedures were approved by Rutgers Institutional Animal Care and Use Committee (#PROTO999900809).

Injection of $RaCl_2$ and inoculation of tumor cells into the tibial marrow

To stratify the biological effects of $^{223}RaCl_2$ on breast cancer cells in a bystander region of the bone marrow versus those cells that receive direct alpha particle irradiation, mice were first injected intravenously with $^{223}RaCl_2$ administered in 200 μL 5 mM citrate buffered saline containing 50 or 600 kBq/kg $^{223}RaCl_2$ (Xofigo®, Cardinal Health). Control mice received only citrate buffered saline. One day after $^{223}RaCl_2$ injection, 80–90% confluent

MDA-MB-231 and MCF-7 cells were labeled with 1 μM CellTracker™ Green CMFDA (ThermoFisher #C7025) in unsupplemented L-15 medium for 45 min. Cells were then trypsinized and their concentration was determined (Coulter ZM, Beckman Coulter). Cells were then centrifuged at 2000 RPM for 3 min in 14 mL conical tubes, medium was aspirated, and the resulting concentrated slurry of cells was placed on ice. Aliquots (3 μL) of 10^6 MDA-MB-231 cells or 4×10^5 MCF-7 cells were loaded into a chilled 31-gauge 10 μL Neuros syringe (Hamilton) kept on ice. The difference in cell number reflects the larger diameter of MCF-7 cells with an emphasis on a fixed 3-μL inoculation volume for both cell lines due to the very small marrow space. Mice were anesthetized with 2% isoflurane in O_2 and a hole was drilled in the tibial marrow compartment with a 29-gauge insulin syringe using a transpatellar approach. The 31-gauge syringe containing the cells was then inserted into the drilled hole and the cells were deposited into the tibial marrow compartment.

Harvesting tibiae and decalcification

At days 1 and 3 following cellular inoculation, mice were anesthetized with 2% isoflurane and injected subcutaneously with 0.2 mL PBS containing 15 mg/mL luciferin (Perkin Elmer #122799). Bioluminescence imaging was performed with an IVIS 200 (Perkin Elmer) to verify a successful intratibial inoculation. Upon visualization, animals were euthanized via cervical dislocation, and tibiae were resected with the muscles and soft tissues completely removed. The resected tibiae were IVIS-imaged to confirm inoculation into the tibial marrow before being fixed in 7 mL of 4% paraformaldehyde (Sigma) in 14 mL round bottom tubes. Samples were fixed for no more than 2 d at 4°C. Following fixation, tibiae were rinsed 3 times in PBS (5 min/rinse) followed by 3 rinses in dH_2O for 5 min. Tibiae were decalcified in 10 mL of 14% EDTA for 2 wk at 4°C on a shaker. The EDTA solution was changed 5 times a week.

Visualizing DNA damage and apoptosis in vivo

Staining for γ-H2AX began with deparaffinizing 5-μm transverse sections as described in Supplementary Data. Deparaffinized sections were heated in a water bath at 95° C for 30 min in 0.01 M citrate buffer and permeabilized with a solution containing 0.2% Triton X-100 (Sigma). Sections were blocked with a solution containing 10% donkey serum (Sigma) and 0.1% Tween 20 (Sigma). Anti-γ-H2AX rabbit antibody (Cell Signaling #9718S) was applied at a 1:400 dilution at 4°C overnight. Secondary antibody conjugated to AlexaFluor568™ (ThermoFisher #A10042) was applied for 1 h at room temperature. Sections were stained with DAPI to visualize the nucleus. Confocal imaging (Nikon A1R Confocal Laser Microscope) used the 488 nm argon laser to excite CellTracker Green™, 405 nm diode laser to excite DAPI, and the 561 nm laser to excite AlexaFluor568™. The 60x oil objective was used to score γ-H2AX foci in all the human breast cancer cells that were present in each transverse cross section, as well as in osteocytes in 3–5 fields of cortical bone imaged to capture at least 100 osteocytes per section.

Assessment of apoptosis by TUNEL staining used the In Situ Cell Death Detection Kit (Sigma #12156792910) according to the manufacturers' protocol. Sections were deparaffinized and pretreated with a permeabilization solution containing 0.1% Triton X-100. DNase treated sections were used as positive controls. Negative control sections

were treated with only the tetramethylrhodamine (TMR) labeling solution. Sections were also stained with DAPI. Imaging was performed similarly to the γ-H2AX stained slides with the 561 nm laser configured to excite TMR.

Stereological determination of tumor location and cell density

Stereological parameters were calculated with guidelines set forth by Peter Mouton using ImageJ software (31). Eight transverse sections (5 μm-thick) were cut from a single tibia per animal inoculated intratibially with either MDA-MB-231 or MCF-7 cells (Supplementary Fig. S1). Sections were obtained from 7 animals per group. The following two-dimensional parameters were calculated: mean cross-sectional tumor diameter, mean cross-sectional cell number, and mean distance from tumor center to the bone surface. The bone surface was defined by the absence of fluorescence in the cortical bone compared to the bone marrow. Values were calculated for each of the 8 sections before being averaged for each animal. Cross-sectional tumor diameter was quantified from 4 distinct linear traversals of the CellTracker Green™-labeled tumor cell population on a given section. The distance from the cross-sectional tumor center to the bone surface was determined by first calculating the cross-sectional tumor midpoint using 6 distinct traversals and identifying the closest point to their intersection.

In addition to two-dimensional parameters, three-dimensional parameters were determined to calculate the cell and packing density. Sections were cut at various depths into the tumor. The cross-sectional area of each section was calculated with a point segmentation method. A two-dimensional, uniformly spaced point grid was overlayed onto each analyzed section. The number of grid points within the tumor was counted and multiplied by 2000 μm^2, the area representing an individual point. The volume of tumor tissue between two sections was estimated by multiplying the distance between the sections (distal end of one section to the proximal end of the other section) by the average area of the two sections (Supplementary Fig. S1). This was repeated for multiple pairs of sections from the same tumor and the resulting regional volumes were summed. The number of cells in each regional volume was determined by dividing the number of cells per section by the fraction of sections sampled in that region (i.e. 1 in every 4 sections sampled resulted in a fraction of 0.25). The resulting regional cell numbers were summed. The total cell number in all the regional volumes was multiplied by a correction factor, C, to account for the fact that, due to their size, cells are located in more than one section (32).

$$C = \frac{\sum_{c=1}^{m} T/(T-d_c)}{\sum_{c=1}^{m} (T-R-S+d_c)/(T-d_c)},$$

where the summation is over cells (c) with average diameter (d_c). R and S are the minimum upper and lower distances the cell could protrude from a section and be counted in a section (0.5 μm each as per Clarke 1993 (32)). T was the thickness of the section. The integer m was the number of cells, in this instance 200, averaged to calculate the correction factor. The cell density for each tumor was calculated by dividing the corrected total cell number by the sum of the regional volumes. The mean cell density for MDA-MB-231 and MCF-7 cells

was obtained by averaging values for tumors in multiple animals. The packing density for MDA-MB-231 and MCF-7 tumors was calculated first by measuring the mean diameter for 200 MDA-MB-231 and MCF-7 tumor cells on 5-μm transverse sections. The mean diameter was used to calculate the mean tumor cell volume. This volume was multiplied by the cell density for the tumor giving the packing density for the tumor. The mean packing density for MDA-MB-231 and MCF-7 cells was obtained by averaging values for tumors in multiple animals.

Quantification of DNA damage and apoptosis

The presence of γ-H2AX foci were scored in three regional cell populations: 1) bystander human breast cancer cells, 2) irradiated human breast cancer cells, and 3) mouse osteocytes. Each human breast cancer cell was measured as being farther or nearer than 70 μm from the bone surface, corresponding to classification as a bystander or irradiated cell, respectively. The bone surface was defined by the absence of fluorescence in the cortical bone compared to the bone marrow. This demarcation was the starting point for 70 μm distances measured into the marrow space. The percentage of cells that were γ-H2AX positive (γ-H2AX$^+$), defined by 1 or more foci, was determined for each population. In addition, the number of foci was classified into three ordinal groups: 1–2 foci, 3–5 foci and 5 or more (5+) foci, representing low, medium, and high levels of DNA damage. Each of these groups was reported as a percentage of total cell population for each of the 3 measured cell populations. For each treatment group and timepoint, 2–7 animals were analyzed using 1–3 sections per animal. Preference was given to sections that ensured at least 100 breast cancer cells were analyzed per animal. For osteocytes, 4–5 fields were used to quantify at least 200 osteocytes per section per animal.

TUNEL-stained sections were quantified as percentage of cells that were positive (TUNEL$^+$). The same three regional populations as those analyzed for γ-H2AX were considered. The percentage of cells that were TUNEL$^+$ at a given timepoint was then divided by the corresponding percentage of TUNEL$^+$ in control animals in the same staining cohort and this ratio was recorded. This was done because TUNEL staining varied greatly between cohorts of animals whose limbs were processed on different days.

Statistical Analysis

Data was graphed and analyzed statistically using Sigma Plot version 14 (Systat Software). Error bars on graphs and notations in the text represent standard error of the mean. Testing for statistical significance between calculated geometric and spatial properties of MDA-MB-231 and MCF-7 was accomplished with a Student's t-test, with $p<0.05$ designating significance. Testing for statistical significance between different groups administered different activities of ^{223}Ra for the effect of administered activity was accomplished with a one-way analysis of variance (ANOVA). A post-hoc Tukey's test was used to test for significance between groups with $p<0.05$ designating significance. If the ANOVA assumptions failed, then a Kruskal-Wallis One Way Analysis of Variance on Ranks was run. A post-hoc Dunn's test was used to test for significance between pairwise comparisons of all groups with $p<0.05$ designating significance.

Absorbed Dose to Tibial Marrow and its Bystander Region

Absorbed doses to the marrow and the bystander region of the marrow were calculated in our earlier publication for complete decay of ^{223}Ra and daughters (30). There we used CT–derived tessellated solids representing the tibia, measurements of activity distribution in the tibia, and Geant4 Monte Carlo simulations. In this work, the tibiae were inoculated with tumor cells 1-day post-administration of $^{223}RaCl_2$ and harvested 1 and 3 days later for histological analysis. Therefore, the absorbed dose to the bystander region to be considered for the day 3 histology is:

$$D = \int_{1d}^{4d} \dot{D}(t=0) e^{-\frac{ln2\, t}{T_e}} dt,$$

where the effective clearance half-time, T_e, is 10.0 d and the initial absorbed dose rate to the bystander region, $\dot{D}(t=0)$, is <0.00012 and <0.0013 Gy/h for the 50 and 600 kBq/kg groups, respectively, as given in Table 1 of Leung *et al.* (30). Integrating yields a maximum absorbed dose of <0.0073 and <0.079 Gy to the bystander region for the 50 and 600 kBq/kg groups, respectively. About 1/3 of the absorbed dose to the bystander region is from beta particles and 2/3 from alpha particles. The absorbed doses for day 1 are about 1/3 of those. The mean absorbed doses to the tibial marrow accumulated from 0 to 4 days are 0.029 and 0.36 Gy for the 50 and 600 kBq/kg groups, respectively. Because this includes tibial marrow within the range of alpha particles emitted from bone, >90% of the absorbed dose is from alpha particles. Tumor cells within the range of alpha particles in the marrow experience a range of doses. The low end of the range is the maximum absorbed dose to the bystander region and the high end of the range is the absorbed dose to the bone. Accordingly, over the first three days postinoculation, the irradiated tumor cells received 0.0073 to 0.32 Gy and 0.079 to 3.7 Gy for the 50 and 600 kBq/kg groups, respectively.

Results:

Geometric and spatial description of the inoculated human breast cancer cells

Human breast cancer cells were found in the tibial marrow both within and beyond the 70-μm maximum range of the alpha particles from the endosteal surface of the bone (Figure 1). The distributions were MDA-MB-231: 49 ± 4.6% irradiated, 51 ± 4.6% bystander, and MCF-7: 61 ± 4.8% irradiated, 39 ± 4.8% bystander.

Serial sections from MDA-MB-231 inoculated mice had a greater mean cross-sectional tumor diameter (250 ± 32 versus 203 ± 29 μm) and significantly greater mean cross-sectional cell count (103 ± 17 versus 54 ±13 cells) than sections taken from MCF-7 inoculated mice. The average distance between the cross-sectional midpoint of the tumor section and the bone surface was longer for the MCF-7 tumors than the MDA-MB-231 tumors (100 ± 24 versus 84 ± 11 μm). The MDA-MB-231 tumors had a significantly higher cell density than MCF-7 tumors ($2.5\times10^{-4} \pm 3.5\times10^{-5}$ versus $1.6\times10^{-4} \pm 1.9\times10^{-5}$ cells/μm^3). However, the MCF-7 tumor cell packing density was 36 ± 4.4% compared to only 28 ± 3.8% for MDA-MB-231. These findings are summarized in Supplementary Table

S1. The totality of these measurements confirmed the presence of bystander populations of MDA-MB-231 and MCF-7 cells.

Increased DNA damage in irradiated and bystander human breast cancer cells

MDA-MB-231 breast cancer cells in both bystander and irradiated regions displayed γ-H2AX foci (Figure 1A–C). The percentages of γ-H2AX$^+$ cells within the irradiated and bystander populations are presented in Figure 2A. At the 1- and 3-day post-inoculation timepoints, the irradiated cells in the 600 kBq/kg group exhibited a significantly higher percentage of cells with DNA damage than the control group. The same was true for the irradiated cells inoculated into the 50 kBq/kg group at the 3-day timepoint. The bystander MDA-MB-231 cells exhibited significantly more DNA damage at the 3-day timepoint for both the 600 kBq/kg and the 50 kBq/kg injected activities of $^{223}RaCl_2$.

Like MDA-MB-231, MCF-7 cells exhibited DNA damage in both bystander and irradiated regions of bone marrow (Figure 1D–F). DNA damage was significant for the irradiated cells in the 600 kBq/kg group compared to the 50 kBq/kg and control groups at both timepoints (Figure 2B). Bystander MCF-7 cells at day 1 post-inoculation in the 600 kBq/kg group were also significantly more susceptible to DNA damage than in control and 50 kBq/kg groups. At day 3, DNA damage in the 600 kBq/kg group was significantly greater than the 50 kBq/kg group. Details regarding the statistical results for both MDA-MB-231 and MCF-7 inoculated cells are summarized in Supplementary Table S2.

Increased DNA damage in mouse osteocytes

Mouse osteocytes showed DNA damage caused by $^{223}RaCl_2$ in the cortical bone (Figure 1G–L). In mice treated with 600 kBq/kg of $^{223}RaCl_2$, the osteocytes underwent significant DNA damage compared to control (Figure 2C). This effect was seen at both 1- and 3-days post tumor cell inoculation, corresponding to 2- and 4-days following injection of $^{223}RaCl_2$. Notably the analysis did not distinguish between mouse osteocytes closer to, or farther from the endosteal and periosteal surfaces. Statistical details are provided in Supplementary Table S2.

Assessment of the extent of DNA damage

Quantification of the extent of DNA damage was performed by categorizing the number of DNA foci per cell into four groups: no apparent damage (0 foci), low damage (1–2 foci), medium damage (3–5 foci), and high damage (>5 foci). These groups were graphed as percentage of the total cell population stratified by irradiated and bystander geospatial regions (Figure 3). Irradiated MDA-MB-231 cells demonstrated significant increases in the percentage of cells showing low and medium damage in the 50 and 600 kBq/kg groups compared to control at day 3 (Figure 3A). Bystander MDA-MB-231 cells exhibited significant increases in medium damage with 50 and 600 kBq/kg treatments as compared to control at day 1, while both treatment levels also exhibited significantly increased low damage at the day 3 timepoint. In contrast MCF-7 irradiated cells demonstrated increased medium and high damage in only the 600 kBq/kg group at day 3 (Figure 3B). Bystander MCF-7 cells displayed significant increases in medium damage at 1 day and small damage at 3 days in the 600 kBq/kg group. Mouse osteocytes in MDA-MB-231 inoculated animals

exhibited significant increases in high damage at 1 day, while having significant increases in cells harboring medium and high damage at 3 days in the 600 kBq/kg group; the results for cells harboring 1–2 foci were significant at day-1 post cell inoculation (Figure 3C). MCF-7-inoculated mice had osteocytes showing significant increases in medium and high damage in 600 kBq/kg treated animals at day 1 (Supplementary Tables S3–S5).

Increased apoptosis in triple negative bystander breast cancer cells

Apoptosis of MDA-MB-231 and MCF-7 cells was observed in irradiated and bystander regions (Figure 4). Quantification was done as the ratio of %TUNEL$^+$ cells in $^{223}RaCl_2$ injected mice to %TUNEL$^+$ cells in control mice at the same timepoint. A significant increase in this ratio was seen in directly irradiated MDA-MB-231 in the 50 and 600 kBq/kg groups at day 1, but not at day 3 (Figure 5A). Bystander MDA-MB-231 cells exhibited significant differences in the ratio between the 50 kBq/kg group and the control group at day 1, and the 600 kBq/kg group and the control group at day 3.

Similarly, the irradiated MCF-7 cells showed significant differences in the ratio for the 600 kBq/kg group at both timepoints, and only on day 3 for the 50 kBq/kg group (Figure 5B). Notably, bystander MCF-7 cells showed no significant differences in the ratio between the various treatment levels and both timepoints (Supplementary Table S6).

Increased apoptosis in mouse osteocytes

For the mouse osteocytes in MDA-MB-231 inoculated animals, significant differences in the relative number of apoptotic osteocytes between both treatment levels were seen at 3-days, but not 1-day post-inoculation (Figure 5C). In contrast, the MCF-7 inoculated animals demonstrated significant differences in the relative number of apoptotic osteocytes between the 600 kBq/kg and control groups only at the 1-day timepoint (Figure 5C).

Discussion:

Radiation therapy is an effective tool for treating cancer. Underscoring this effectiveness, is the classical paradigm of radiation biology that the important biological effects of ionizing radiation (e.g., mutations, oncogenic transformation, cell death) result from energy deposition on or near the DNA strands. Accumulating evidence, however, has prominently implicated radiation induced bystander effects as also facilitating these biological changes (33). Much of the research quantifying radiation induced bystander effects was done *in vitro*. Although a very early study removed tumors from mice, X-irradiated the animals, and returned the tumors to their hosts (34). The controls were irradiated without their tumors being removed. The unirradiated tumor grafts shrank by fifty percent and the animals lived for roughly five weeks, whereas members of the control group died shortly after one week. Animal studies done by Brooks *et al.* in the 1970s may have been among the first to show alpha-particle induced bystander effects *in vivo* (35). There have been additional *in vivo* studies including our previous work that established an *in vivo* model to study the impact of radiation-induced bystander effects on DTC growth delay caused by $^{223}RaCl_2$ (30). The present work stratifies the direct effects of alpha particles emitted by $^{223}RaCl_2$

from the radiation-induced bystander effects using direct histological measurements of their biological effects at the individual cell level *in vivo*.

Measurements of biological events at the cellular level is important given the heterogeneity of cell irradiation in radiopharmaceutical therapy. Unlike with external beam therapy, different cells in the tumor may receive different absorbed doses (36). We have established previously an *in vivo* model in which both MDA-MB-231 and MCF-7 xenografts exist within and beyond the range of alpha particles in the tibial cortical bone (30). Tumor cells close to the bone receive absorbed doses more than an order of magnitude greater than cells distant from bone. Recently, we have also established that the radiosensitivities of the two cell lines are similar both for gamma rays and alpha particles (Supplementary Fig. S2). Here we show that there were no significant differences in mean tumor diameter or distance from tumor center to bone surface between MDA-MB-231 and MCF-7 cells (Supplementary Table S1). There were significant differences in cross-sectional tumor cell count and cell density (cells/μm^3), however these differences were not unexpected given the inherent cell size disparity. Therefore, these factors can neither explain the distinctive bystander cell biological responses nor the differences in long-term growth delays.

In relating long-term growth delay to cellular level biological effects, DNA damage was found to be widespread in the bystander cell populations of both MDA-MB-231 and MCF-7 breast cancer cells. Both MCF-7 and MDA-MB-231 cells are genomically unstable and, as expected, both were found to have high endogenous expression of γ-H2AX foci although most tumor cells contained no foci. MDA-MB-231 cells inoculated intracardially that migrated to bone were previously found by others to have an increase in DNA damage in mice pretreated with $^{223}RaCl_2$ (8). However, that study did not distinguish between irradiated and bystander MDA-MB-231 cells. The incidence of DNA damage seen in our bystander cells mirrored that in irradiated cells, suggesting that bystander effects play an important role in the response of these cancer cells to $^{223}RaCl_2$. Consistent with this suggestion, in a recently published study, bystander effects caused by radioimmunotherapy with alpha particle emitters were found to be responsible for 50% of the observed cell death (37). Oxidative stress was also important in mediating the bystander effects from alpha particle emitters. In the present study, bystander MDA-MB-231 cells required only 50 kBq/kg of $^{223}RaCl_2$ to cause significant elevation of DNA damage and the damage was similar to that observed for the 600 kBq/kg group. However, the bystander MCF-7 cells needed 600 kBq/kg to impart a significant elevation of DNA damage. This contrasts their dependencies on administered activity for long-term growth delay of the tumor cell xenografts (30). In our growth delay experiments, 600 kBq/kg was required to cause growth delay of the MDA-MB-231 bystander and irradiated cells, whereas MCF-7 bystander and irradiated cells responded in a dose-dependent manner. The noticeable difference in DNA damage and growth delay responses between MDA-MB-231 and MCF-7 cells may result from intrinsic differences in their ER statuses; MCF-7 cells are ER^+ while MDA-MB-231 cells are ER^-. Prior work found that while MDA-MB-231 had a higher radiosensitivity than MCF-7 cells to irradiation by helium-3 ions as measured by micronuclei formation, the nonirradiated, bystander MCF-7 cells formed more micronuclei than the nonirradiated, bystander MDA-MB-231 cells (38). These authors also found that 17β-estradiol (E2) treatment enhanced the bystander effect and the production of reactive oxidative species

in MCF-7 cells, but not MDA-MB-231 cells. Further experimental work may discern the effect of ER status and E2 on the radiation-induced bystander DNA damage observed in this study.

The difference in response to DNA damage between MDA-MB-231 and MCF-7 cells may also result from intrinsic genetic differences. Central to the DNA damage response is the tumor suppressor protein p53 (39). MDA-MB-231 cells have a mutant copy of *TP53* while MCF-7 cells have wildtype *TP53* (40). This difference in p53 status has previously illustrated that MDA-MB-231 cells were induced less into senescence than MCF-7 cells following gamma irradiation of MCF-7 (41). The observed dose-dependent differences in bystander damage combined with genetic differences in DNA repair machinery may be additive or synergistic. The result may influence MCF-7 inoculated cells to delay replication. This may be a reason for the greater long-term growth delay seen for MCF-7 cells in our previous work (30). While the p53 pathway is involved in the response of cells receiving bystander signals, there is also evidence it may be part of the production of bystander signals as well. The mice in our work presented herein were wildtype for *Trp53*. Experiments comparing a systemic antitumor effect in wildtype *Trp53* with *Trp53* null mice by Camphausen *et al.* found that p53 mediated an abscopal effect leading to shrinkage of tumors distant from the site of irradiation (42). Additional work found that irradiated bone marrow from wildtype p53 mice, but not from p53 null mice, produced inflammatory cytokines that could induce a bystander effect via medium transfer experiments (43). Furthermore, a multicellular co-culture system demonstrated that p53 was central to human lung cell production of proapoptotic signals that were mediated by human macrophages and directed to bystander human lymphoblasts (44). In contrast, p53 was also found to be unnecessary for bystander signaling in medium transfer experiments involving human colon tumor cells (45). However, another research group found that the addition of serotonin to medium transferred from these irradiated human colon tumor cells resulted in bystander effects only when the irradiated donor cells were *TP53* wildtype and not *TP53* null (46). Work by Shao et al. showed that mutant *TP53* malignant glioma cells were able to induce bystander effects leading to chromosomal damage via nitric oxide signaling when exposed to energetic helium-3 ions (47). Future studies may investigate whether p53 contributes to the radiation-induced bystander DNA damage observed in this study considering the *p53* status of both the irradiated, intermediary, and bystander cell populations.

Further assessment of DNA damage extent was quantified by the number of γ-H2AX foci. Bystander cancer cells were found to have significant increases in low (1–2 foci) and medium (3–5 foci) damage, whereas irradiated cancer cells had significant increases in high damage (5+ foci) as well. DNA damage foci are widely used as a marker for genotoxic insults caused by direct effects of radiation, as well as radiation-induced bystander effects (48). Direct irradiation with alpha particles emitted by $^{223}RaCl_2$ creates clustered DNA damage in the nucleus (49) which is difficult to repair and can fuel systemic inflammatory effects (50). There is evidence that the clustered DNA damage caused by high-LET radiation is mediated through large repair centers and is not proportional to absorbed doses (51). The DNA repair machinery of the cell is overworked as it attempts to repair multiple breaks in the same cluster (52). Repair of multiple breaks in the same cluster was shown to be hindered by exposure to lower LET radiation (53). Cultured human fibroblasts were exposed

to X rays, alpha particles, or a mixed field of X rays and alpha particles, over a range of absorbed doses spanning between 0.2 and 0.8 Gy. The fibroblasts exposed to the mixed radiation field were less likely to produce large foci characteristic of a cellular response to densely ionizing radiation. Furthermore, the large foci in the fibroblasts exposed to a mixed radiation field disappeared more slowly than corresponding cells exposed to alpha particles (53). Our results show that chronic irradiation with $^{223}RaCl_2$ creates significant increases in high damage in breast cancer cells close to the bone, within range of the alpha and beta particles, up to 3 days following their inoculation. This effect was dose-dependent in both cell lines as was the growth delay observed previously in MCF-7 tumor xenografts (30). In the present work, these breast cancer cells, designated as being in a directly irradiated region of the bone marrow, received absorbed doses of 0.0073–0.32 Gy (50 kBq/kg) and 0.079–3.7 Gy (600 kBq/kg) from alpha particle and beta particle irradiation over the three-day period as estimated with dose rates from our previous work (30). These irradiated breast cancer cells are exposed not only to alpha particles but also lower LET beta particles. High LET radiation has been found, however, to induce clustered DNA damage at doses ranging from 0.1 to 1.0 Gy (54). The identified highly complex DNA damage persisting in the tumor cells closer to the bone may serve as one source for signals transmitted to bystander cells (Figure 6). Longer follow up studies on the number and size of DNA damage foci seen in MDA-MB-231 and MCF-7 cells closer to the bone surface may help explain differences in tumor growth delay previously observed. Additional work on the repair kinetics of each cell line in response to $^{223}RaCl_2$ would be also valuable.

Beyond significant increases in high DNA damage in irradiated tumor cells, the significant increase in low and medium damage observed in the bystander cells, up to 3 days after inoculation, is conspicuous. There was a dose-dependence to this effect with MCF-7 cells needing 600 kBq/kg of $^{223}RaCl_2$ to cause significant elevation of low and medium DNA damage, whereas bystander MDA-MB-231 cells needed only 50 kBq/kg. The progeny of bystander cells from cocultures with cells exposed to high LET radiation were previously seen to have higher levels of micronuclei (55). Identifying the sources of these bystander cell DNA damages is a crucial next step. These bystander DNA damages may be generated from chronic, genotoxic signaling by irradiated cancer cells close to bone, irradiated marrow cells close to bone, or irradiated osteocytes in the bone (Figure 6). Further work may clarify the duration of the DNA damage in these bystander cells. Understanding the duration and extent of DNA damage in bystander cells may help distinguish between the growth delays experienced by MDA-MB-231 and MCF-7 cells, and thereby give further insight into how cell growth is related to treatment regimens in the clinical setting.

Lastly, the response of osteocytes was assessed in response to $^{223}RaCl_2$. Osteocytes, while being the master regulators of bone homeostasis, facilitate tumor progression into the mineralized tissue (16). Their response to high-LET alpha particles is not well characterized. The current work presents one of the first *in vivo* examinations of the biological effects of high-LET radiation on osteocytes. Mouse osteocytes had significant increases in DNA damage and apoptosis with exposure to $^{223}RaCl_2$. Osteocyte apoptosis is well known to stimulate the process of bone turnover with coupled bone resorption and new bone formation. This increase in bone turnover is a hallmark of osteoblastic and osteolytic tumor formation (16). However, osteocyte communication may also mitigate tumor proliferation.

There is increasing interest in the direct and indirect signaling of osteocytes that can positively and negatively impact tumor cells (56–58). Understanding the role of osteocytes in propagating radiation induced bystander effects caused by $^{223}RaCl_2$ is important given that the radionuclide settles within the mineralized bone and osteocytes are capable of interacting with the marrow space and blood vessel via their dendritic processes (13,14). It is therefore necessary to include osteocytes in addition to osteoblasts and osteoclasts as part of the bone microenvironment targeted by $^{223}RaCl_2$ (Figure 6). Suominen *et al.* have attributed cytotoxic effects of $^{223}RaCl_2$ to direct irradiation of osteoclasts, osteoblasts, and cancer cells (9). Bystander effects were not considered, yet the data presented here indicate that bystander effects are present in the cancer cells. Future work will be needed to identify the direct and indirect intercellular signaling events mediating these bystander effects. Nonetheless these bystander effects appear to contribute substantially to the reduction in tumor progression previously seen by our group (30). Thus, the action of ^{223}Ra on a bone marrow microenvironment, infiltrated with cancer cells, must account for direct effects on tumor cells and all bone cell types as well as bystander effects (Figure 6).

Understanding of the bystander effect imparted by $^{223}RaCl_2$ and other alpha particle emitters is of potentially great value therapeutically. The ability to eliminate disseminated tumor cells that have circulated from the primary tumor represents a powerful treatment approach for metastatic cancer. The alpha particles emitted by ^{223}Ra have a short range, thereby sparing normal tissue but also bystander cancer cells. This work demonstrates that ^{223}Ra induces biological effects in the form of DNA damage and apoptosis to these bystander cancer cells. While ^{223}Ra decay does involve the production of daughter radionuclides that emit alpha particles, beta particles, and gamma rays, bystander tumor cells only received absorbed doses of <0.0073 and <0.079 Gy for the 50 and 600 kBq/kg groups, respectively. Given these low absorbed doses and the preponderance of low and medium DNA damage observed in the bystander tumor cells, this strongly suggests that bystander effects are the predominant reason for the observed biological effects. Therefore, $^{223}RaCl_2$ could provide additional clinical benefit by inducing biological effects in tumor cells considered outside the range of alpha particles emitted by ^{223}Ra. However, careful patient-selection is warranted because $^{223}RaCl_2$ also induced significant increases in bone osteocyte DNA damage and apoptosis. Therefore, in advance of treatment with $^{223}RaCl_2$, patients who have an increased risk for secondary tumor formation from alpha particle emitters, like ^{223}Ra, must be identified. Radiation-induced bystander effects is likely to be a factor in the therapeutic efficacy of new radiopharmaceuticals as well (59,60). Radiopharmaceuticals, in particular $^{223}RaCl_2$, have the potential for systemic radiation treatment of metastatic breast and prostate cancer (61). Providing clinical researchers with biomarkers has been suggested to facilitate improved patient selection in trials with $^{223}RaCl_2$ (62,63). Expanding these biomarkers by identifying the cellular networks and key events in pathways implicated in the propagation of cytotoxic effects to tumor cells outside the range of high LET radiation could provide a more holistic treatment approach to metastatic breast and prostate cancer that spreads to bone. Treatments combining $^{223}RaCl_2$ with other therapies are of increasing interest for use against metastatic prostate cancer (64). These combinatorial approaches may be enhanced by examining the propagation of cytotoxic effects to tumor cells outside the

range of the alpha particles. This would be also of benefit to the quality and quantity of life for patients undergoing treatment for metastatic prostate cancer with $^{223}RaCl_2$.

In summary, this study demonstrates that alpha particles emitted by $^{223}RaCl_2$ in bone induce, in the bone marrow, DNA damage and apoptosis in disseminated breast cancer cells that lie beyond the ~70 μm range of the alpha particles. These bystander breast cancer cells suffer similar biological consequences as their neighboring irradiated cancer cells. This supports the concept that radiation induced bystander effects contribute to the therapeutic efficacy of alpha particle emitters. In addition, this work reveals that irradiation of bone by $^{223}RaCl_2$ induces DNA damage and apoptosis in osteocytes. Taken together, the effects of $^{223}RaCl_2$ on bystander breast cancer cells and osteocytes highlight a multifactorial impact of $^{223}RaCl_2$ on the bone microenvironment. Further consideration is warranted for $^{223}RaCl_2$ as a systemic treatment of disseminated breast cancer cells in bone through direct irradiation and radiation induced bystander effects. This supports clinical investigation of the efficacy of $^{223}RaCl_2$ to prevent breast cancer DTC from progressing to oligometastases.

Supplementary Material

Refer to Web version on PubMed Central for supplementary material.

Acknowledgments

This study was supported in part by research funding from National Institutes of Health (NIH) 1R01CA198073 to R. Howell and E. Azzam, New Jersey Commission on Cancer Research (NJCCR) DFHS17PPC029 to B. Canter, and NJCCR DFHS15PPC009 to C. Leung. Special thanks to Luke Fritzky of the Confocal Imaging Facility and Joel Pierre of the Histology Core Facility for their assistance and advice in preparing and imaging tissue sections.

References

1. Wan L, Pantel K, Kang Y. Tumor metastasis: moving new biological insights into the clinic. Nat Med2013;19(11):1450–64 doi 10.1038/nm.3391. [PubMed: 24202397]
2. Kluetz PG, Pierce W, Maher VE, Zhang H, Tang S, Song P, et al. Radium Ra 223 dichloride injection: U.S. Food and Drug Administration drug approval summary. Clinical cancer research : an official journal of the American Association for Cancer Research2014;20(1):9–14 doi 10.1158/1078-0432.CCR-13-2665. [PubMed: 24190979]
3. Parker C, Nilsson S, Heinrich D, Helle SI, O'Sullivan JM, Fossa SD, et al. Alpha emitter radium-223 and survival in metastatic prostate cancer. The New England journal of medicine2013;369(3):213–23 doi 10.1056/NEJMoa1213755. [PubMed: 23863050]
4. Henriksen G, Fisher DR, Roeske JC, Bruland OS, Larsen RH. Targeting of osseous sites with alpha-emitting ^{223}Ra: comparison with the beta-emitter ^{89}Sr in mice. J Nucl Med2003;44(2):252–9. [PubMed: 12571218]
5. Larsen RH, Saxtorph H, Skydsgaard M, Borrebaek J, Jonasdottir TJ, Bruland OS, et al. Radiotoxicity of the alpha-emitting bone-seeker ^{223}Ra injected intravenously into mice: histology, clinical chemistry and hematology. In vivo2006;20(3):325–31. [PubMed: 16724665]
6. Ritter MA, Cleaver JE, Tobias CA. High-LET radiations induce a large proportion of non-rejoining DNA breaks. Nature1977;266(5603):653–5 doi 10.1038/266653a0. [PubMed: 859634]
7. Henriksen G, Breistol K, Bruland OS, Fodstad O, Larsen RH. Significant antitumor effect from bone-seeking, alpha-particle-emitting (223)Ra demonstrated in an experimental skeletal metastases model. Cancer Res2002;62(11):3120–5. [PubMed: 12036923]
8. Suominen MI, Rissanen JP, Kakonen R, Fagerlund KM, Alhoniemi E, Mumberg D, et al. Survival benefit with radium-223 dichloride in a mouse model of breast cancer bone metastasis. Journal of the National Cancer Institute2013;105(12):908–16 doi 10.1093/jnci/djt116. [PubMed: 23682134]

9. Suominen MI, Fagerlund KM, Rissanen JP, Konkol YM, Morko JP, Peng Z, et al. Radium-223 Inhibits Osseous Prostate Cancer Growth by Dual Targeting of Cancer Cells and Bone Microenvironment in Mouse Models. Clinical cancer research : an official journal of the American Association for Cancer Research2017;23(15):4335–46 doi 10.1158/1078-0432.CCR-16-2955. [PubMed: 28364014]
10. Marquart KH. Early ultrastructural changes in osteocytes from the proximal tibial metaphysis of mice after the incorporation of ^{224}Ra. Radiat Res1977;69(1):40–53. [PubMed: 834854]
11. Bonewald LF. Osteocytes as dynamic multifunctional cells. Ann N Y Acad Sci2007;1116:281–90 doi 10.1196/annals.1402.018. [PubMed: 17646259]
12. Dallas SL, Prideaux M, Bonewald LF. The osteocyte: an endocrine cell … and more. Endocr Rev2013;34(5):658–90 doi 10.1210/er.2012-1026. [PubMed: 23612223]
13. Delgado-Calle J, Anderson J, Cregor MD, Hiasa M, Chirgwin JM, Carlesso N, et al. Bidirectional Notch Signaling and Osteocyte-Derived Factors in the Bone Marrow Microenvironment Promote Tumor Cell Proliferation and Bone Destruction in Multiple Myeloma. Cancer Res2016;76(5):1089–100 doi 10.1158/0008-5472.CAN-15-1703. [PubMed: 26833121]
14. Kamel-ElSayed SA, Tiede-Lewis LM, Lu Y, Veno PA, Dallas SL. Novel approaches for two and three dimensional multiplexed imaging of osteocytes. Bone2015;76:129–40 doi 10.1016/j.bone.2015.02.011. [PubMed: 25794783]
15. Bonewald LF. The Role of the Osteocyte in Bone and Nonbone Disease. Endocrinol Metab Clin North Am2017;46(1):1–18 doi 10.1016/j.ecl.2016.09.003. [PubMed: 28131126]
16. Atkinson EG, Delgado-Calle J. The Emerging Role of Osteocytes in Cancer in Bone. JBMR Plus2019;3(3):e10186 doi 10.1002/jbm4.10186. [PubMed: 30918922]
17. Shiozawa Y. The Roles of Bone Marrow-Resident Cells as a Microenvironment for Bone Metastasis. Adv Exp Med Biol2020;1226:57–72 doi 10.1007/978-3-030-36214-0_5. [PubMed: 32030676]
18. Maroni P, Bendinelli P. Bone, a Secondary Growth Site of Breast and Prostate Carcinomas: Role of Osteocytes. Cancers (Basel)2020;12(7) doi 10.3390/cancers12071812.
19. Little JB. Genomic instability and bystander effects: a historical perspective. Oncogene2003;22(45):6978–87. [PubMed: 14557801]
20. Belyakov OV, Mitchell SA, Parikh D, Randers-Pehrson G, Marino SA, Amundson SA, et al. Biological effects in unirradiated human tissue induced by radiation damage up to 1 mm away. Proc Natl Acad Sci U S A2005;102(40):14203–8 doi 10.1073/pnas.0505020102. [PubMed: 16162670]
21. Mitchell SA, Randers-Pehrson G, Brenner DJ, Hall EJ. The bystander response in C3H 10T1/2 cells: the influence of cell-to-cell contact. Radiat Res2004;161(4):397–401. [PubMed: 15038773]
22. Howell RW, Rajon D, Bolch WE. Monte Carlo simulation of irradiation and killing in three-dimensional cell populations with lognormal cellular uptake of radioactivity. International journal of radiation biology2012;88(1–2):115–22 doi 10.3109/09553002.2011.602379. [PubMed: 21745001]
23. Boyd M, Ross SC, Dorrens J, Fullerton NE, Tan KW, Zalutsky MR, et al. Radiation-induced biologic bystander effect elicited in vitro by targeted radiopharmaceuticals labeled with alpha-, beta-, and auger electron-emitting radionuclides. J Nucl Med2006;47(6):1007–15. [PubMed: 16741311]
24. Autsavapromporn N, de Toledo SM, Little JB, Jay-Gerin JP, Harris AL, Azzam EI. The role of gap junction communication and oxidative stress in the propagation of toxic effects among high-dose alpha-particle-irradiated human cells. Radiat Res2011;175(3):347–57 doi 10.1667/RR2372.1. [PubMed: 21388278]
25. Desai S, Srambikkal N, Yadav HD, Shetake N, Balla MM, Kumar A, et al. Molecular Understanding of Growth Inhibitory Effect from Irradiated to Bystander Tumor Cells in Mouse Fibrosarcoma Tumor Model. PLoS One2016;11(8):e0161662 doi 10.1371/journal.pone.0161662. [PubMed: 27561007]
26. Mothersill C, Lyng F, Seymour C, Maguire P, Lorimore S, Wright E. Genetic factors influencing bystander signaling in murine bladder epithelium after low-dose irradiation in vivo. Radiat Res2005;163(4):391–9 doi 10.1667/rr3320. [PubMed: 15799694]

27. Szatmari T, Kis D, Bogdandi EN, Benedek A, Bright S, Bowler D, et al. Extracellular Vesicles Mediate Radiation-Induced Systemic Bystander Signals in the Bone Marrow and Spleen. Front Immunol2017;8:347 doi 10.3389/fimmu.2017.00347. [PubMed: 28396668]
28. Szatmari T, Persa E, Kis E, Benedek A, Hargitai R, Safrany G, et al. Extracellular vesicles mediate low dose ionizing radiation-induced immune and inflammatory responses in the blood. International journal of radiation biology2019;95(1):12–22 doi 10.1080/09553002.2018.1450533. [PubMed: 29533121]
29. Hall EJ, Hei TK. Genomic instability and bystander effects induced by high-LET radiation. Oncogene2003;22(45):7034–42 doi 10.1038/sj.onc.1206900. [PubMed: 14557808]
30. Leung CN, Canter BS, Rajon D, Back TA, Fritton JC, Azzam EI, et al. Dose-Dependent Growth Delay of Breast Cancer Xenografts in the Bone Marrow of Mice Treated with ^{223}Ra: The Role of Bystander Effects and Their Potential for Therapy. J Nucl Med2020;61(1):89–95 doi 10.2967/jnumed.119.227835. [PubMed: 31519805]
31. Mouton PR. Principles and Practices of Unbiased Stereology: An Introduction for Bioscientists. Baltimore: Johns Hopkins University Press; 2002. 214 p.
32. Clarke PG. An unbiased correction factor for cell counts in histological sections. J Neurosci Methods1993;49(1–2):133–40 doi 10.1016/0165-0270(93)90117-a. [PubMed: 8271826]
33. Heeran AB, Berrigan HP, O'Sullivan J. The Radiation-Induced Bystander Effect (RIBE) and its Connections with the Hallmarks of Cancer. Radiat Res2019;192(6):668–79 doi 10.1667/RR15489.1. [PubMed: 31618121]
34. Murphy JB, Morton JJ. The Effect of Roentgen Rays on the Rate of Growth of Spontaneous Tumors in Mice. J Exp Med1915;22(6):800–3 doi 10.1084/jem.22.6.800. [PubMed: 19867960]
35. Brooks AL, Retherford JC, McClellan RO. Effect of $^{239}PuO_2$ particle number and size on the frequency and distribution of chromosome aberrations in the liver of the Chinese hamster. Radiat Res1974;59(3):693–709. [PubMed: 4428016]
36. Neti PV, Howell RW. Log normal distribution of cellular uptake of radioactivity: implications for biologic responses to radiopharmaceuticals. J Nucl Med2006;47(6):1049–58. [PubMed: 16741316]
37. Ladjohounlou R, Lozza C, Pichard A, Constanzo J, Karam J, Le Fur P, et al. Drugs That Modify Cholesterol Metabolism Alter the p38/JNK-Mediated Targeted and Nontargeted Response to Alpha and Auger Radioimmunotherapy. Clinical cancer research : an official journal of the American Association for Cancer Research2019;25(15):4775–90 doi 10.1158/1078-0432.CCR-18-3295. [PubMed: 31061069]
38. Shao C, Folkard M, Held KD, Prise KM. Estrogen enhanced cell-cell signalling in breast cancer cells exposed to targeted irradiation. BMC Cancer2008;8:184 doi 10.1186/1471-2407-8-184. [PubMed: 18590532]
39. Jin S, Levine AJ. The p53 functional circuit. J Cell Sci2001;114(Pt 23):4139–40. [PubMed: 11739646]
40. Neve RM, Chin K, Fridlyand J, Yeh J, Baehner FL, Fevr T, et al. A collection of breast cancer cell lines for the study of functionally distinct cancer subtypes. Cancer Cell2006;10(6):515–27 doi 10.1016/j.ccr.2006.10.008. [PubMed: 17157791]
41. Mirzayans R, Andrais B, Scott A, Wang YW, Murray D. Ionizing radiation-induced responses in human cells with differing TP53 status. Int J Mol Sci2013;14(11):22409–35 doi 10.3390/ijms141122409. [PubMed: 24232458]
42. Camphausen K, Moses MA, Menard C, Sproull M, Beecken WD, Folkman J, et al. Radiation abscopal antitumor effect is mediated through p53. Cancer Res2003;63(8):1990–3. [PubMed: 12702593]
43. Lorimore SA, Rastogi S, Mukherjee D, Coates PJ, Wright EG. The influence of p53 functions on radiation-induced inflammatory bystander-type signaling in murine bone marrow. Radiat Res2013;179(4):406–15 doi 10.1667/RR3158.2. [PubMed: 23578188]
44. Fu J, Zhu L, Tu W, Wang X, Pan Y, Bai Y, et al. Macrophage-Mediated Bystander Effects after Different Irradiations through a p53-dependent Pathway. Radiat Res2020;193(2):119–29 doi 10.1667/RR15354.1. [PubMed: 31841081]

45. Mothersill C, Bristow RG, Harding SM, Smith RW, Mersov A, Seymour CB. A role for p53 in the response of bystander cells to receipt of medium borne signals from irradiated cells. International journal of radiation biology2011;87(11):1120–5 doi 10.3109/09553002.2011.610866. [PubMed: 21831006]
46. Kalanxhi E, Dahle J. The role of serotonin and p53 status in the radiation-induced bystander effect. International journal of radiation biology2012;88(10):773–6 doi 10.3109/09553002.2012.711919. [PubMed: 22803606]
47. Shao C, Folkard M, Michael BD, Prise KM. Bystander signaling between glioma cells and fibroblasts targeted with counted particles. Int J Cancer2005;116(1):45–51 doi 10.1002/ijc.21003. [PubMed: 15756683]
48. Rothkamm K, Barnard S, Moquet J, Ellender M, Rana Z, Burdak-Rothkamm S. DNA damage foci: Meaning and significance. Environ Mol Mutagen2015;56(6):491–504 doi 10.1002/em.21944. [PubMed: 25773265]
49. Costes SV, Chiolo I, Pluth JM, Barcellos-Hoff MH, Jakob B. Spatiotemporal characterization of ionizing radiation induced DNA damage foci and their relation to chromatin organization. Mutat Res2010;704(1–3):78–87 doi 10.1016/j.mrrev.2009.12.006. [PubMed: 20060491]
50. Mavragani IV, Nikitaki Z, Souli MP, Aziz A, Nowsheen S, Aziz K, et al. Complex DNA Damage: A Route to Radiation-Induced Genomic Instability and Carcinogenesis. Cancers (Basel)2017;9(7) doi 10.3390/cancers9070091.
51. Neumaier T, Swenson J, Pham C, Polyzos A, Lo AT, Yang P, et al. Evidence for formation of DNA repair centers and dose-response nonlinearity in human cells. Proc Natl Acad Sci U S A2012;109(2):443–8 doi 10.1073/pnas.1117849108. [PubMed: 22184222]
52. Staaf E, Brehwens K, Haghdoost S, Czub J, Wojcik A. Gamma-H2AX foci in cells exposed to a mixed beam of X-rays and alpha particles. Genome Integr2012;3(1):8 doi 10.1186/2041-9414-3-8. [PubMed: 23121736]
53. Yu T, MacPhail SH, Banath JP, Klokov D, Olive PL. Endogenous expression of phosphorylated histone H2AX in tumors in relation to DNA double-strand breaks and genomic instability. DNA Repair (Amst)2006;5(8):935–46 doi 10.1016/j.dnarep.2006.05.040. [PubMed: 16814620]
54. Sutherland BM, Bennett PV, Sidorkina O, Laval J. Clustered DNA damages induced in isolated DNA and in human cells by low doses of ionizing radiation. Proc Natl Acad Sci U S A2000;97(1):103–8 doi 10.1073/pnas.97.1.103. [PubMed: 10618378]
55. de Toledo SM, Buonanno M, Harris AL, Azzam EI. Genomic instability induced in distant progeny of bystander cells depends on the connexins expressed in the irradiated cells. International journal of radiation biology2017;93(10):1182–94 doi 10.1080/09553002.2017.1334980. [PubMed: 28565963]
56. Zhou JZ, Riquelme MA, Gao X, Ellies LG, Sun LZ, Jiang JX. Differential impact of adenosine nucleotides released by osteocytes on breast cancer growth and bone metastasis. Oncogene2015;34(14):1831–42 doi 10.1038/onc.2014.113. [PubMed: 24837364]
57. Zhou JZ, Riquelme MA, Gu S, Kar R, Gao X, Sun L, et al. Osteocytic connexin hemichannels suppress breast cancer growth and bone metastasis. Oncogene2016 doi 10.1038/onc.2016.101.
58. Ma YV, Lam C, Dalmia S, Gao P, Young J, Middleton K, et al. Mechanical regulation of breast cancer migration and apoptosis via direct and indirect osteocyte signaling. J Cell Biochem2018 doi 10.1002/jcb.26745.
59. Morgenstern A, Apostolidis C, Kratochwil C, Sathekge M, Krolicki L, Bruchertseifer F. An Overview of Targeted Alpha Therapy with ^{225}Actinium and ^{213}Bismuth. Curr Radiopharm2018;11(3):200–8 doi 10.2174/1874471011666180502104524. [PubMed: 29732998]
60. Sathekge M, Bruchertseifer F, Knoesen O, Reyneke F, Lawal I, Lengana T, et al. ^{225}Ac-PSMA-617 in chemotherapy-naive patients with advanced prostate cancer: a pilot study. Eur J Nucl Med Mol Imaging2019;46(10):129–138 doi 10.1007/s00259-019-04401-9. [PubMed: 30232539]
61. Sgouros G, Bodei L, McDevitt MR, Nedrow JR. Radiopharmaceutical therapy in cancer: clinical advances and challenges. Nat Rev Drug Discov2020;19(9):589–608 doi 10.1038/s41573-020-0073-9. [PubMed: 32728208]

62. Den RB, George D, Pieczonka C, McNamara M. Ra-223 Treatment for Bone Metastases in Castrate-Resistant Prostate Cancer: Practical Management Issues for Patient Selection. Am J Clin Oncol2019;42(4):399–406 doi 10.1097/COC.0000000000000528. [PubMed: 30844849]

63. Schumann S, Eberlein U, Muhtadi R, Lassmann M, Scherthan H. DNA damage in leukocytes after internal ex-vivo irradiation of blood with the alpha-emitter Ra-223. Sci Rep2018;8(1):2286 doi 10.1038/s41598-018-20364-7. [PubMed: 29396412]

64. Morris MJ, Corey E, Guise TA, Gulley JL, Kevin Kelly W, Quinn DI, et al. Radium-223 mechanism of action: implications for use in treatment combinations. Nat Rev Urol2019;16(12):745–56 doi 10.1038/s41585-019-0251-x. [PubMed: 31712765]

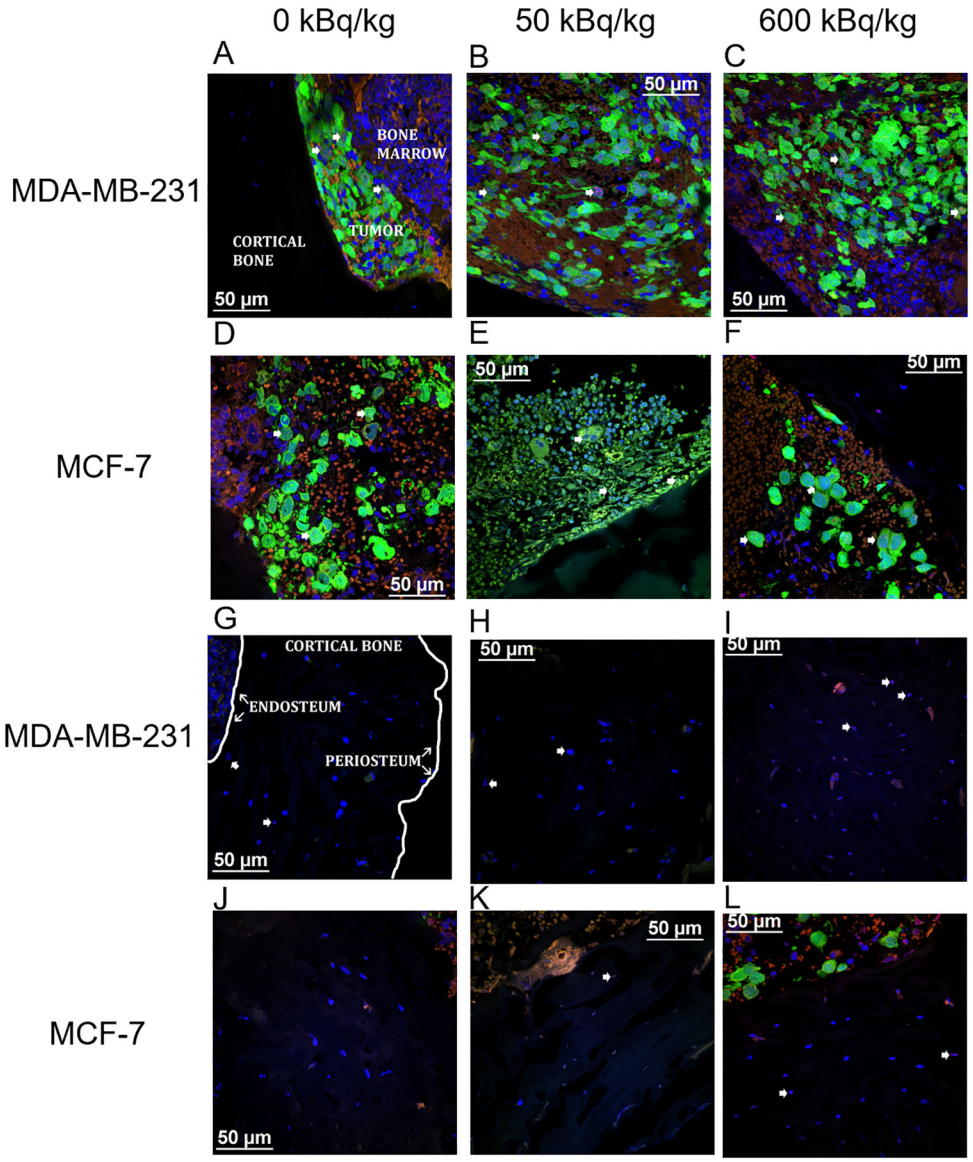

Figure 1. Representative confocal microscopic images of transverse tibial bone marrow sections containing human breast cancer cells that were inoculated into animals pre-treated with ^{223}Ra dichloride and assayed for γ-H2AX formation.

MDA-MB-231 (A–C) and MCF-7 (D–F) labeled with CellTracker™ Green CMFDA and stained with anti-γ-H2AX antibody (AlexaFluor™ 568 red) to visualize DNA damage. The tumor, bone marrow, and cortical bone have all been demarcated (A). Nuclear counter-staining with DAPI (blue) visualizes DNA damage in mouse osteocytes in the tibiae of animals inoculated with MDA-MB-231 cells (G–I) and MCF-7 cells (J–L). The inner (endosteum) and outer (periosteum) cell layers surrounding the cortical bone have been noted (G). Arrowheads delineate γ-H2AX positive cells. Images acquired with a Nikon A1R microscope with CFI Apochromat TIRF 60XC oil (NA 1.40), DS-Fi3 camera and NIS-Elements C software.

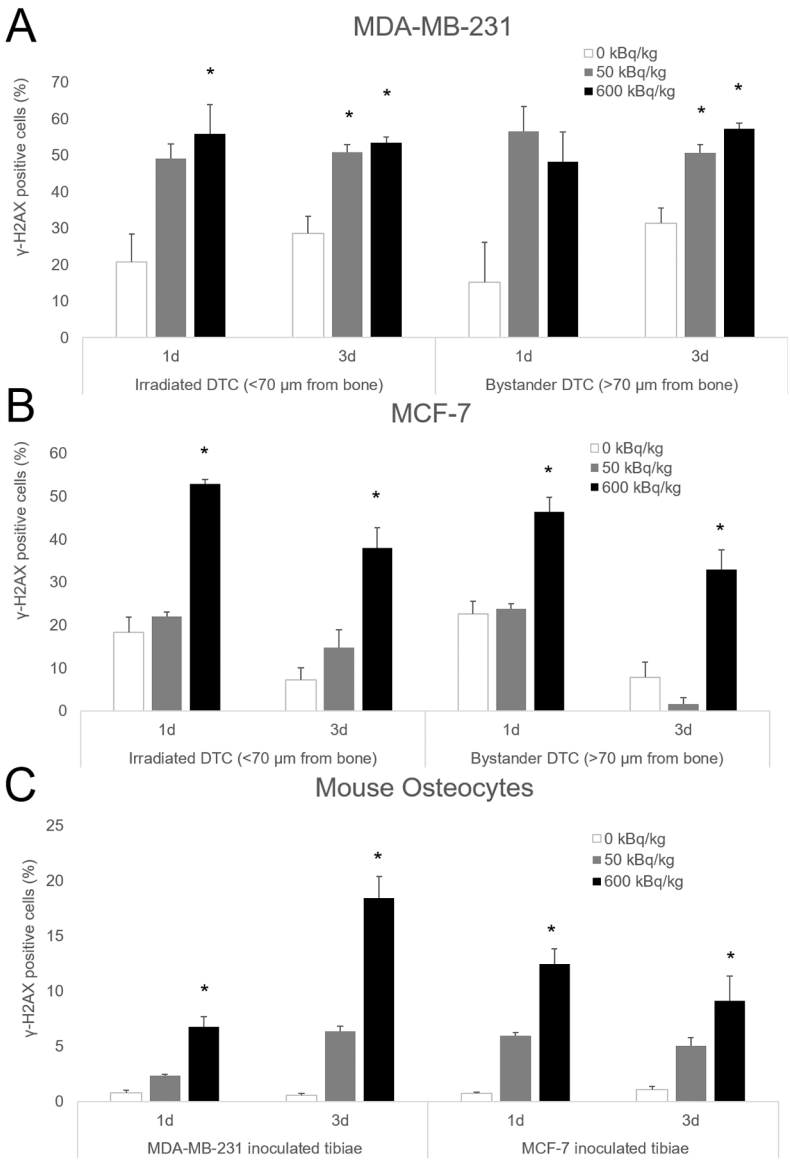

Figure 2. Quantification of DNA damage in transverse tibial bone marrow sections stained with anti-γ-H2AX antibody from mice inoculated with human breast cancer cells.

MDA-MB-231 (A), MCF-7 human breast cancer cells (B), as well as mouse osteocytes (C) from both groups. Mice were sacrificed 1 and 3 days following cell inoculation after previously being treated with 50 or 600 kBq/kg of $^{223}RaCl_2$. Control mice were given saline. Irradiated disseminated tumor cells were demarcated from bystander disseminated tumor cells by being less than or greater than 70 μm from the inner surface of the cortical bone. The percentage of γ-H2AX positive disseminated tumor cells and mouse osteocytes were determined from 1–3 sections for each animal with n=2–7 per group. Errors bars represent Standard Error of the Mean (SEM) with asterisks denoting significance (see Supplementary Table S2).

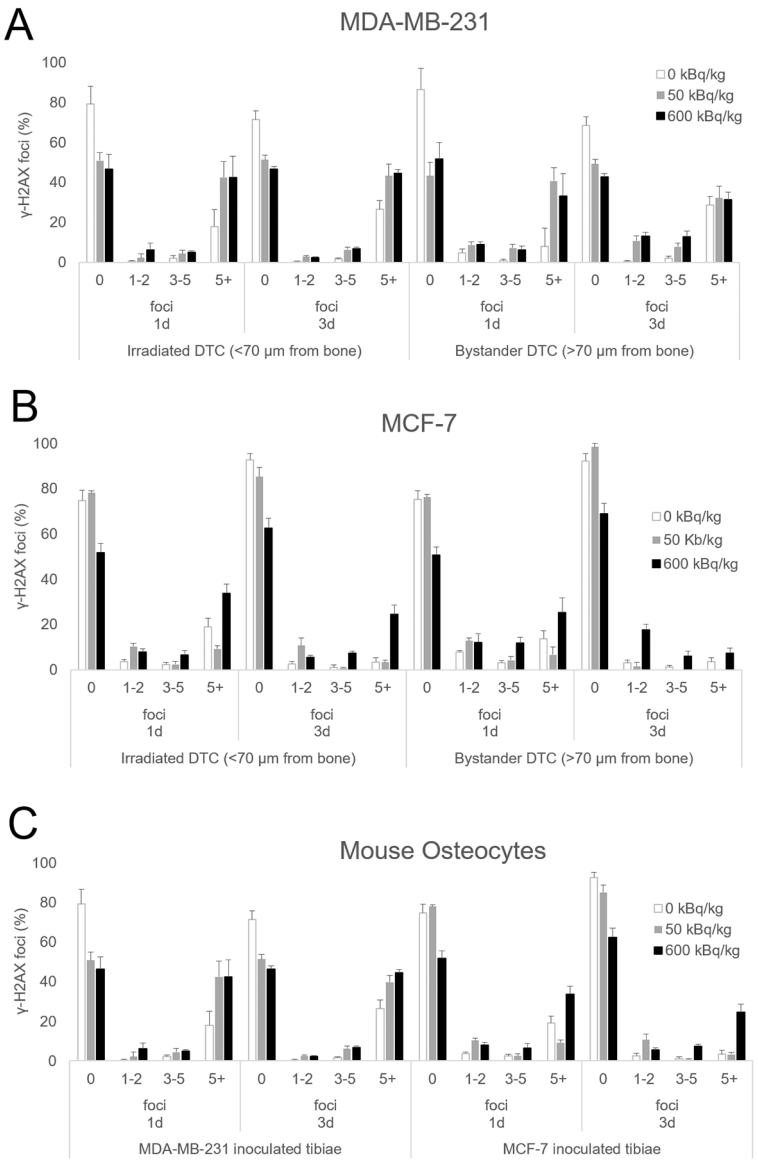

Figure 3. Quantification of the quality of DNA damage visualized with anti-γ-H2AX antibody from mice inoculated with human breast cancer cells.

MDA-MB-231 (A), MCF-7 human breast cancer cells (B), as well as mouse osteocytes (C) from both groups. Mice were sacrificed 1 and 3 days following cell inoculation after previously being treated with 50 or 600 kBq/kg of $^{223}RaCl_2$. Control mice were given saline. Irradiated disseminated tumor cells were demarcated from bystander disseminated tumor cells by being less than or greater than 70 μm from the inner surface of the cortical bone. The percentage of γ-H2AX positive disseminated tumor cells and mouse osteocytes were counted from 1–3 sections for each animal with n=2–7 per group with the quality of DNA damage quantified through counting the number of γ-H2AX foci in a cell presenting DNA damage. 1–2 foci represented small DNA damage with 3–5 marking medium DNA damage while 5+ foci indicated large DNA damage. Errors bars represent Standard Error of the Mean (SEM) and statistical significances are reported in Supplementary Tables S3–S5.

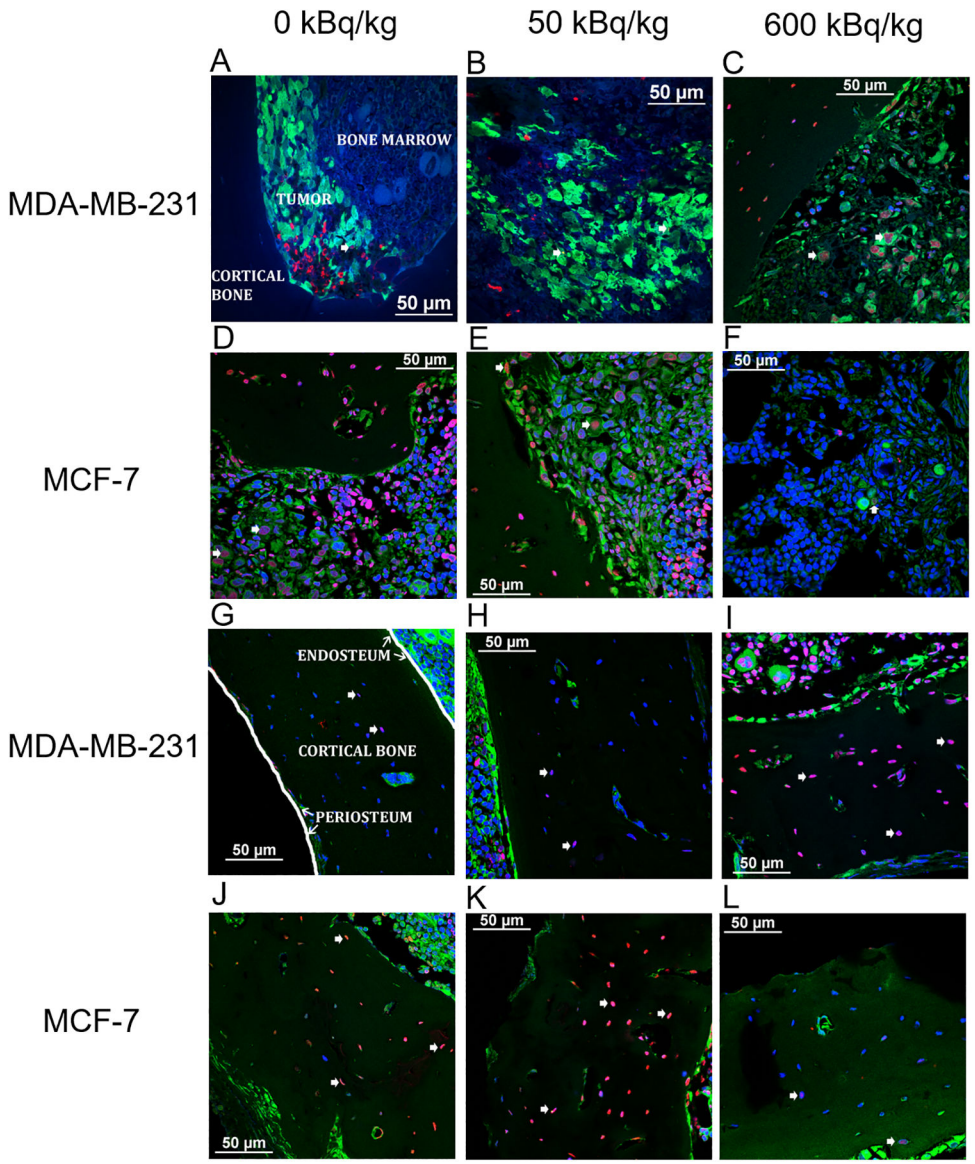

Figure 4. Representative confocal microscopic images of apoptosis in transverse tibial bone marrow sections containing human breast cancer cell lines.

MDA-MB-231 (A–C), and MCF-7 (D–F) (green) stained with TUNEL (red) visualizing apoptosis. Nuclear counter-staining with DAPI (blue) also allows for visualizing apoptosis in mouse osteocytes from animals inoculated with MDA-MB-231 cells (G–I) and MCF-7 cells (J–L).

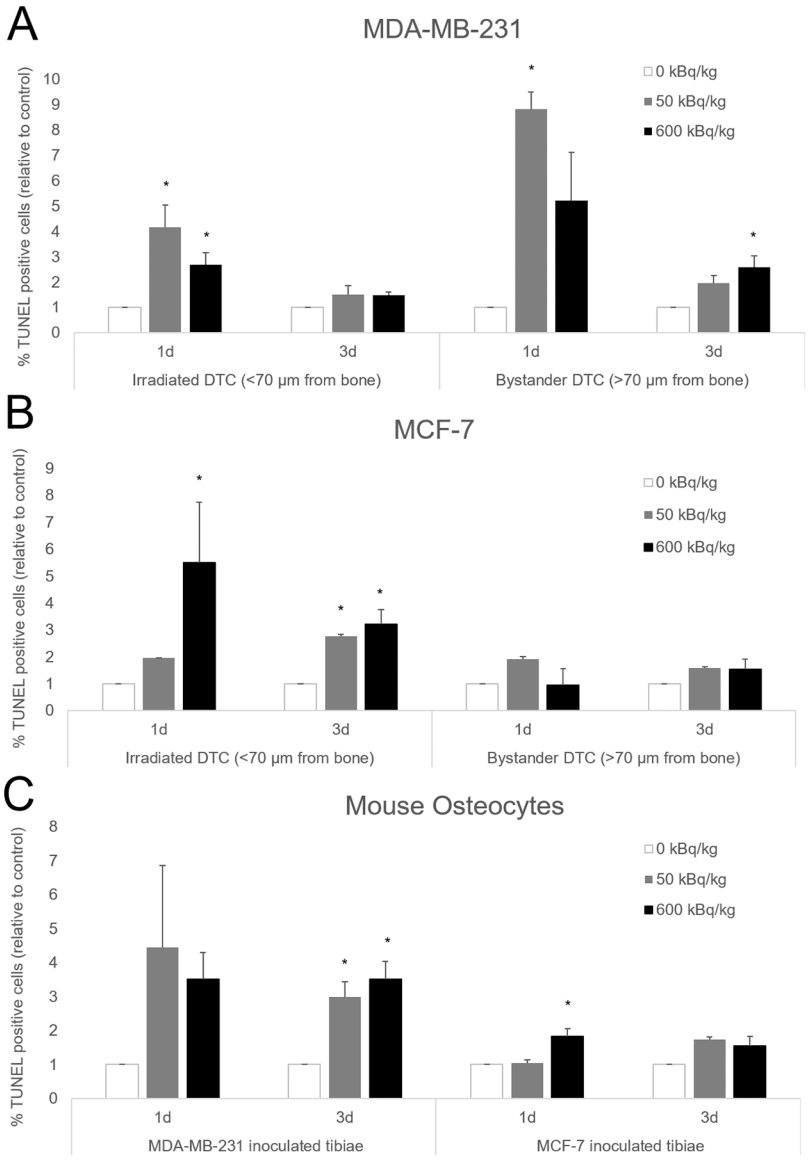

Figure 5. Quantification of apoptosis in transverse tibial bone marrow sections stained with TUNEL from mice inoculated with human breast cancer cells.

MDA-MB-231 (A), MCF-7 human breast cancer cells (B), as well as mouse osteocytes (C) from both groups. Mice were euthanized 1- and 3-days following cell inoculation after previously being treated with 50 or 600 kBq/kg of $^{223}RaCl_2$. Control mice were given saline. Irradiated disseminated tumor cells were demarcated from bystander disseminated tumor cells by being less than or greater than 70 μm from the inner surface of the cortical bone. The percentage of TUNEL positive disseminated tumor cells and mouse osteocytes were determined from 1–3 sections for each animal with n=2–7 per group. That percentage of TUNEL positive cells was then normalized to a percentage of TUNEL positive cells from a control animal that had their tissue processed and embedded at the same time. Errors bars represent Standard Error of the Mean (SEM) with asterisks denoting significance (see Supplementary Table S6).

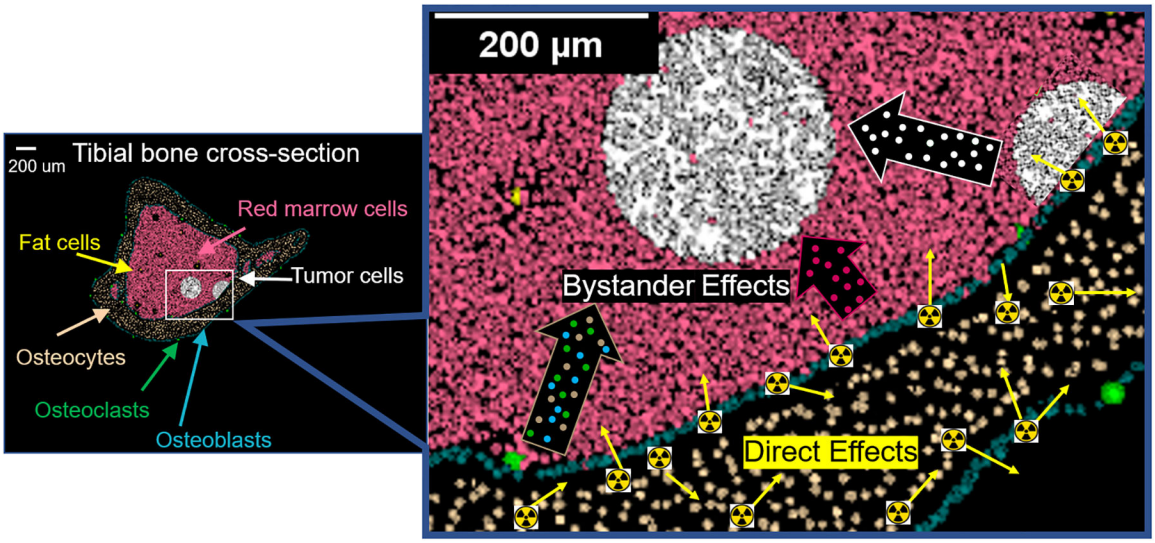

Figure 6. Visual overview of a dual effect of ^{223}Ra on disseminated tumor cells in bone.

Direct effects from alpha particle irradiation (yellow arrows in magnified image) contribute to biological changes detected histologically in disseminated tumor cells and osteocytes within the range of the alpha particles. *Bystander effects* also contribute to biological changes in tumor cells beyond the range of the alpha particles emitted from the endosteal surface of the bone. These bystander effects can arise from tumor cells (white outlined arrow) and marrow cells (pink outlined arrow) within the range of alpha particles, and bone cells (brown outlined arrow). The presented data indicate ^{223}Ra elicits bystander effects in the bone environment, which likely contribute to the previously observed growth delay of the disseminated tumor cells as described by Leung *et al.* (30).